Journal of Molecular Structure 1217 (2020) 128483

Contents lists available at ScienceDirect

Journal of Molecular Structure

journal homepage: http://www.elsevier.com/locate/molstruc

Regioselectivity of reduction of nitro groups in 3, 5-dinitrosalicylic acid monohydrate explored by experimental and theoretical charge density analysis

Arshad Mehmood [a], Aisha Fahim [a], Maqsood Ahmed [b], Sajida Noureen [b, *]

[a] Department of Chemistry & Biochemistry, Texas Christian University, Fort Worth, Texas, 76129, USA
[b] Materials Chemistry Laboratory, Department of Chemistry, The Islamia University of Bahawalpur, Baghdad-ul-Jadeed Campus, 63100, Pakistan

ARTICLE INFO

Article history:
Received 26 October 2019
Received in revised form
6 May 2020
Accepted 18 May 2020
Available online 19 May 2020

ABSTRACT

Preferential reduction of one of the two nitro groups in 3, 5-dinitrosalicylic acid monohydrate has been investigated using experimental charge density analysis from a high-resolution X-rays diffraction data at 100K combined with DFT theoretical calculations. The structure was refined using the classical Independent Atom Model as well as the Multipolar Atom Model. Bond characterization is performed in terms of charge density distribution and the associated topological properties. The theoretical (B3LYP/6-311++G(d,p), SMD/water) electrostatic potential molecular surfaces and atomic charges complimented the mechanism where one of the two nitro groups with higher negative charge gets preferentially reduced. The weak intermolecular interactions and hydrogen bonding are further quantified by the Hirshfeld surface analysis.

1. Introduction

Nitroaromatics comprise an important class of chemicals due to their wide use in agrochemicals, textile dyes, munitions and other industrial applications [1,2]. They are categorized as potential environmental contaminants [3] and considerable interest has been devoted to understand their fate in soil and aquatic environment [4]. Polynitroaromatics are observed to undergo regioselective reductive transformations to aromatic amines that are resistant to further reduction [5,6]. It has been reported that the rate of reduction of the first nitro group, in these compounds, is much more rapid than the rate of reduction of subsequent nitro groups, which is sometimes so slow that the process is effectively stopped after the reduction of the first nitro group [1]. The knowledge of selective reduction and ability to predict the regioselectivity of the reduction process is fundamental to understand the fate and environmental impacts of various reduced products of ploynitroaromatics [2]. In this context, the reduction regioselectivities of various polynitroaromatics have been studied experimentally in aqueous media [7–23] and observed selectivities have also been rationalized by the results of quantum mechanical calculations using Density Functional Theory (DFT) [9,18,20] and Austin Model 1-Solvation Model 2 (AM1—SM2) [1]. However, the regioselectivities of these compounds have not been gleaned from structural studies like the analysis of the experimentally and theoretically derived groundstate electron densities. Charge density analysis can be used to get insight into the chemical reactivity of a molecule [24–27]. In addition, there is also significant current interests to understand the effects of non-covalent intermolecular interactions on the reactivity of chemical systems [28]. On one hand these diverse interactions can organize reagents in space, activate a covalent bond, provide a suitable environment and can drive the energetic patterns of chemical reaction [29] and on the other hand, their significant role is recognized in the stabilization of the supramolecular architecture, crystal packing, and molecular recognition [30–36]. Among these interactions, strong hydrogen bonds, for example, O–H···O, N–H···O, and N–H···N are generally recognized as the most energetically important [36–38]. However, the importance of weak interactions such as C···H, N···H, and H···H etc. has also been explored [35,39,40]. The analysis of these interactions in crystals of polynitroaromatics is proposed to be equally useful to quantify their regioselective reduction.

3,5-Di-nitrosalicylic acid (DNSA) is an example of polynitroaromatics having both carboxyl and hydroxyl groups [41]. DNSA provides one of the best chemical synthons for the

* Corresponding author.
E-mail address: Sajida.Noureen@iub.edu.pk (S. Noureen).

https://doi.org/10.1016/j.molstruc.2020.128483
0022-2860/

construction of hydrogen-bonded structural motifs [42–44]. It protonates most of nitrogen Lewis bases giving compounds with significantly enhanced crystallinity through hydrogen bonding [45] and its charge-transfer and proton-transfer complexes have been extensively synthesized [41,45]. The regioselective reduction of one nitro group of DNSA under alkaline conditions is used to detect the reducing sugars in urine and to quantify the carbohydrates levels in blood using the colorimetric methods [46–48] (Scheme 1).

In this study, we report experimental and theoretical charge density analysis of monohydrate form of DNSA using high resolution X-rays diffraction data collected at 100K. The aim of the study is to calculate the electron density derived properties of the molecule and to make the qualitative and quantitative analysis of covalent and non-covalent interactions and to compare the results obtained from the experiment with the high level theoretical methods. An insight into the regioselective reduction of DNSA is also gained by theoretical (B3LYP/6-311++G (d,p)) electrostatic potential molecular surfaces and atomic charges calculated in the gas phase and continuum water (SMD/water). In addition, the nitro groups in most of the nitroaromatics are nearly coplanar with the benzene ring [49,50], in DNSA, one of the two nitro groups is twisted out of the aromatic plane approximately 51°, which provides an additional opportunity to understand the electron density distribution on C–N bond in this class of polynitroarmatics.

2. Experimental

2.1. Crystallization and data collection

Light yellow elongated block shaped crystals of DNSA were grown from the slow evaporation of an aqueous solution at room temperature. A highly diffracting single crystal of the compound with dimensions 0.283 × 0.236 × 0.213 mm^3 was selected under the microscope. The crystal was mounted on the goniometer using Paratone-N oil (cryoprotectant) on the tip of MiTeGen MicroLoops LD™, 45 mm away from the detector and was cooled to a temperature of 100 (2) K under the flow of liquid nitrogen using Oxford Cryosystem [51]. High resolution data sets up to a sinθ/λ 1.02 $Å^{-1}$ were collected on a Bruker D8 Quest diffractometer with a Photon 100 CMOS detector with an average redundancy of 9 and completeness of ~100% using a scan angle of 0.5°/frame and exposure times of 40 s. The Bragg intensities were indexed with APEX3 software [52]. An analytical absorption correction was applied using the real face indices using SADABS [53]. Table 1 gives the crystal and data collection details.

2.2. Structure solution and IAM refinement using SHELXL

The crystal structure was solved by direct methods using SIR92 [54] and initially refined using SHELXL [55] in the WinGX [56] package. All H atoms were located from the difference Fourier analysis. The H atoms attached to carbon were fixed using a riding model whereas those attached to oxygen atoms were refined freely. The atomic displacement parameters were refined, isotopically for H atoms and anisotropically for non-hydrogen atoms. Thermal ellipsoid plots and atom numbering are shown in Fig. 1 and a summary of refinement statistics is provided in Table 1.

2.3. The Independent Atom Model (IAM) refinement using MoPro

The refined structure using SHELXL was imported to MoPro [57] for full matrix least square refinement. First of all, only the scale factor was refined and then the fractional coordinates of all the atoms were refined. Initially, the bond lengths involving C–H atoms were constrained to standard neutron distances from the International Tables of Crystallography [58], whereas those attached to oxygen atoms were refined freely. After convergence of the IAM refinement, the atomic coordinates were used as initial geometry to optimize the solid state structure using Gaussian 09 package [59] at PBEPBE/6-311G(d,p) level of theory at periodic boundary conditions (PBC). The optimised distances from high level DFT calculations were used to restrain the bond lengths of all H atoms to a freedom of 0.002 Å in this refinement and in the subsequent multipolar model refinement. Subsequently, the parameters of thermal motion of all the atoms were refined anisotropically. The realistic multipole densities requires anisotropic thermal displacement parameters for H atoms in the refinement [60–63]. The anisotropic thermal parameters of hydrogen atoms were calculated using the SHADE server [64] and were fixed during refinement. In order to have a goodness of fit close to unity, a weighting scheme $w = 1/[\sigma^2 (Fo^2)+(aP)^2+bP]$ where $P=(Fo^2+2Fc^2)/3$ with $a = 0.047$ and $b = 0.056$ was adopted. The software DRKplot [65] was used to optimize the weighting scheme. The normal probability plot is shown in the supporting information Fig. S1.

In the beginning, only high order reflections sin θ/λ > 0.6 $Å^{-1}$ were used for refinement to properly deconvolute the atomic positions from thermal motion. Then a simple refinement using all reflections was carried out. An I/σ cut-off of 2 was applied throughout the process of refinement. At the end of the IAM refinement, the conventional *R* factor was 2.70%, the weighted *R* factor was 6.9% and the goodness-of-fit parameter was found to be 1.03 (Table 1). The residual electron density map after the IAM refinement is shown in Fig. 2(A) which shows that the electron density peaks are clearly centered on the bonds as well as on the lone pairs.

2.4. The multipolar model (MM) refinement using MoPro

The crystal structures resulting from the IAM refinement was used as a starting point for multipolar refinement with MoPro program [57]. The Hansen and Coppens multipolar formalism [66] was used to represent the charge density distribution (Equation (1)).

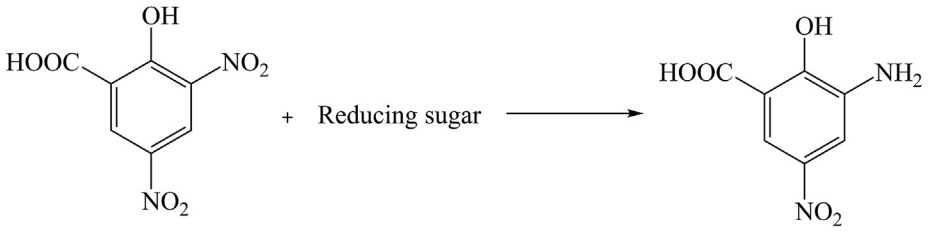

Scheme 1. Mechanism of regioselective reduction of one nitro group of DNSA by the reducing sugars.

Table 1
Experimental details.

Crystal data	
Chemical formula	$C_7H_6N_2O_8$
M_r	246.12
Crystal system, space group	Monoclinic, *I*2
Temperature (K)	100(2)
a, *b*, *c* (Å)	12.3643(4), 5.8123(2), 12.9859(5)
β (°)	101.050(3)
V (Å^3)	915.93(6)
Z	4
Radiation type	Mo *Kα*
μ (mm^{-1})	0.17
Crystal size (mm)	0.28 × 0.24 × 0.21
Data collection	
Diffractometer	Bruker Kappa Apex II CMOS detector
Absorption correction	Analytical (*SADABS* [53];
T_{min}, T_{max}	0.717, 0.749
No. of measured, independent and observed [> 2.0σ(*I*)] reflections	72436, 8090, 7734
R_{int}	0.025
$(\sin\theta/\lambda)_{max}$ (Å^{-1})	1.020

Refinement	(Multipolar)	(IAM_MoPro)
$R[F^2 > 2\sigma(F^2)]$, $wR(F^2)$, *S*	0.019, 0.041, 1.06	0.027, 0.071, 1.07
Total No. of reflections	8090	8090
No. of reflections used after I/σ > 2	7665	7665
No. of parameters	763	102
No. of restraints	8	6
H-atom treatment	H-atom parameters were restrained to optimised DFT values with a freedom of 0.002 Å	H-atom parameters were restrained to optimised DFT values with a freedom of 0.002 Å
$\Delta\rangle_{max}$, $\Delta\rangle_{min}$ (e Å^{-3})	0.231, −0.216	0.50, −0.35

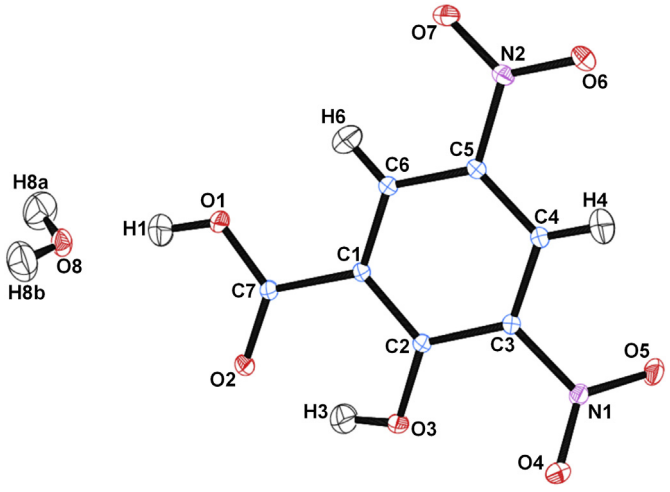

Fig. 1. A thermal ellipsoid diagram drawn at 50% probability showing the atom numbering scheme.

$$\rho(\vec{r}) = \rho_{core}(r) + P_{val}\kappa^3\rho_{val}(\kappa r) + \sum_{l=0}^{l_{max}} \kappa'^3 R_{n_l}(\kappa' r) \sum_{m=0}^{l} P_{lm} y_{lm} \pm (\theta, \phi) \quad (1)$$

This model describes the electron density of an atom as a sum of three different terms. The first two terms are spherically averaged core and valence electron densities of the atom and the last term corresponds to non-spherical part of the valence electron density which is given in terms of real spherical harmonic functions $Y_{lm\pm}$. P_{val} represents the valence population and $P_{lm\pm}$ are the multipole populations. κ and κ′ are the parameters of contraction and expansion for the valence and multipole populations respectively. R_l are the radial Slater-type functions. A full matrix least square refinement was carried out against F^2 using all the reflections up to a sinθ/λ of 1.02 Å^{-1}. The refinement strategy was the following:

1. At the first stage, the scale factor, fractional coordinates and thermal displacement parameters of all non-H atoms were successively refined and H atoms were treated as described previously.
2. The parameters of contraction (κ) of Hansen and Coppens equation were refined for all non-hydrogen atoms whereas for hydrogen atoms the values of κ and κ′ were restrained to 1.13 (0.02) and 1.20 (0.02) [67].
3. This was followed by the refinement of valence population of all atoms.
4. All the multipoles were refined followed by the refinement of parameters of expansion (κ′). The H atoms were refined to dipolar level whereas the rest of the atoms were refined to octapolar level.

At the end of the MM refinement, the conventional *R* factor was 1.9%, the weighted *R* factor was 4.1% and the goodness of fit parameter was found to be 1.06 (Table 1). After the multipolar refinement, there is significant difference in the residual density values between IAM (0.50, −0.35 eÅ^{-3}) and MM (0.231, −0.216 eÅ^{-3}). The fractal dimensions plot for the multipolar model has also been included in Fig. S6 in supporting information which shows that the residual maxima and minima have been evenly distributed. The residual electron density map after the MM refinement is shown in Fig. 2(B) which is quite featureless.

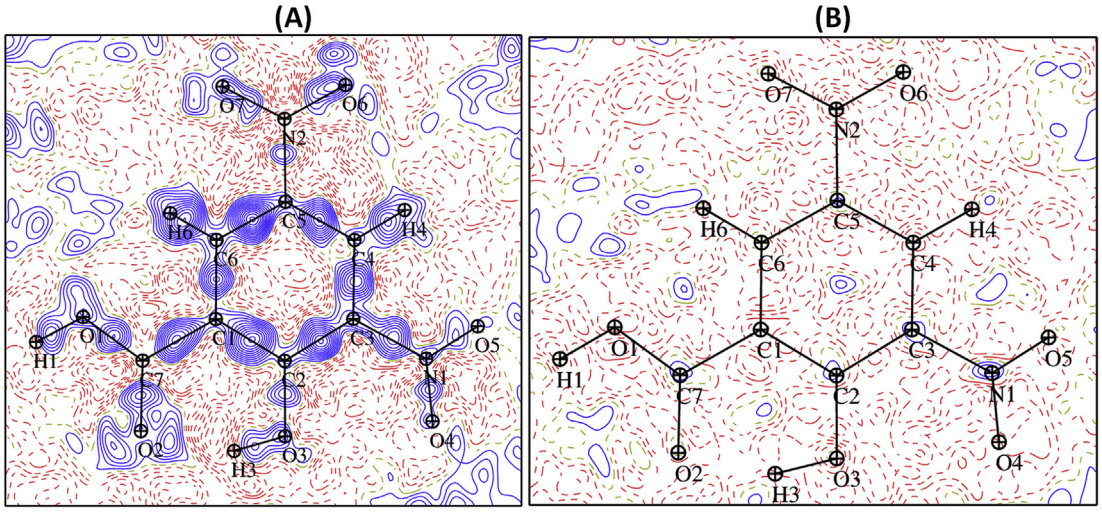

Fig. 2. Residual electron density maps drawn after IAM (A) and Multipolar (B) refinements. Contour level = 0.05e/Å^3.

2.5. Theoretical calculations

Three types of theoretical calculations were carried out using Gaussian [59] suite of programs.

A. Gas-phase calculations are carried out at the experimental and optimised geometries using Kohn-Sham density functional theory (DFT) with the B3LYP exchange-correlation functional [68]. Molecular orbitals are expanded in the 6-311++G(2d,2p) basis set [69] and no corrections are made for basis set superposition error. The molecular wave function is obtained at this level of theory where the calculations are performed using quadratically convergent SCF procedures [70]. The pro-molecular and deformation density, integrated theoretical population and atomic volume were obtained using the Multiwfn program [71]. To avoid the orientation dependence problem in pro-molecular density, the calculated electron density of each atom was artificially spehericalized. The calculation of Bond Critical Points (BCPs) and theoretical topological properties at BCPs, the Laplacian distributions, atomic basin, and gradient paths were calculated using AIM-UC program [72].

B. Solid phase periodic calculations of DNSA were performed for geometry optimization to get precise positions of hydrogen atoms using PBEPBE [73] functional and 6-311G(d,p) basis set.

C. It has been proposed in previous studies [1] that the first step of regioselective reduction of polynitro-aromatics involves a one electron reduction to form a radical anion. Hence gas phase and continuum water (SMD) [74] phase single molecule calculations were performed on DNSA radical anion with and without water molecule using wB97XD/6-311++g(d,p) level of theory. The calculated electrostatic potential of the optimised structures at global minima, in gas and aqueous phase, is coloured mapped onto the 0.001 electrons/Å^3 isosurface of the electron density. The results were used to visualize the localization of negative charge on the particular nitro group, which influences the selectivity of the site of protonation during the reduction process.

3. Results and discussion

3.1. Molecular and crystal structure

The oxygen atoms attached to nitro groups as well as the carbonyl oxygen atom deviate from the molecular plane. The deviation shown by the oxygen atoms of the N1 nitro group is more pronounced to avoid steric hindrance with the hydroxyl group. The C2—C3—N1—O5 torsion angle is 146.62 (3)° whereas the N2 nitro group is relatively co-planer with the aromatic ring with the C6—C5—N2—O6 torsion angle is 175.49(3)°. The H1 and H3 atoms also slightly deviate from the plane of the molecule due to involvement in strong hydrogen bond formation. There are two molecules in the asymmetric unit (One DNSA moiety and one water moiety) and eight molecules in the unit cell. Fig. S2, shows the molecular packing along *a* and *b* axes. The stacked layers of the molecules are spread in a two dimensional '*fishing net*' arrangement.

The molecular assembly is rich in intermolecular interactions. The crystal structure is stabilized by a number of H bonds (Table 2) and van der Waals interactions. The molecular surface contains a number of H bond donor and acceptor sites. Every oxygen atom is involved in the formation of atleast one intermolecular contact. The hydroxyl group (O1) of the carboxylic moiety forms strong hydrogen bonds in terms of distance with a water molecule which serve to bridge a three dimensional network of the molecules. The O2 atom forms an intramolecular hydrogen bond at a very short distance by accepting the H3 atom of the O3 hydroxyl group. The O3 atom also makes a weak intermolecular H bond by donating its H atom to the O5 atom of the neighbouring molecule (-*x*+1/2, *y*-1/2, -*z*+3/2) at a distance of 2.43 Å. The O4 atom forms a close contact with the O6 atom of a neighbouring molecule (*x*, *y*-1, *z*). The O5 atom forms a bifurcated contact with an adjacent molecule (-*x*+1/2, *y*-1/2, -*z*+1), one with the O2 atom and the other being the formation of a hydrogen bond by accepting the H3 atom. Similarly the O6 atom also forms a bifurcated interaction, on one hand it makes a contact with the O4 atom of adjacent molecule (*x*, *y*+1, *z*) and on the other, it accepts the H8A atom of the water molecule (-*x*+1, *y*+1, -*z*+1). The water molecule plays a bridging role in the molecular

Table 2
Hydrogen-bond geometry (Å, °) for Multipolar model.

D—H···*A*	*D*—H	H···*A*	*D*···*A*	*D*—H···*A*
O3—H3···O5^{i}	1.01	2.43 (1)	3.0243 (3)	117 (1)
O3—H3···O2	1.01	1.60 (1)	2.5423 (2)	152 (1)
O1—H1···O8	1.02	1.51 (1)	2.5199 (2)	173 (1)
C4—H4···O5^{ii}	1.08	2.55 (1)	3.2577 (3)	123 (1)
O8—H8*A*···O6^{iii}	0.98	2.06 (1)	3.0020 (3)	161 (1)
O8—H8*B*···O2^{iv}	0.97	1.84 (1)	2.8085 (2)	178 (1)

Symmetry codes: (i) -*x*+1/2, *y*-1/2, -*z*+3/2; (ii) -*x*, *y*, -*z*+1; (iii) -*x*+1, *y*-1, -*z*+1; (iv) -*x*+3/2, *y*+1/2, -*z*+3/2.

assembly by holding together four adjacent DNSA molecules through a network of O—H···O hydrogen bonds. It accepts H1 hydrogen atom from the parent DNSA molecule with H···O distance of 1.505 Å. It donates H8B atom to O2^{i} (*i* = -*x*+1/2, *y*+1/2, -*z*+1/2) atom of the carboxylic group of an adjacent molecule at a distance 1.979 Å. Similarly it donates H8A atom to the O6^{ii} (*ii* = -*x*+1, *y*-1, -*z*+1) atom of the nitro group of another adjacent molecule at a H···O distance of 2.059 Å. There is also an interaction between O8 and the O1 atoms at a distance of 3.03 Å (Fig. 3).

3.2. Hirshfeld surface analysis

The Hirshfeld surfaces [75–80] in the crystal structure are constructed based on the electron density distributions calculated as the sum of the spherical atom electron densities. Every given crystal structure has a unique Hirshfeld surface and this lends a possibility of getting both qualitative and qu-anti-tative insight into the inter-molecular inter-actions of the molecular crystal [81]. The Hirshfeld surfaces were generated using Crystal Explorer 3.1 [82] based on the findings from X-ray analysis in which H atom bond distances were optimised using periodic DFT calculations.

A Hirshfeld surface enables the identification of the regions of particular importance to intermolecular inter-actions. The value of d_{norm} is negative (red colour) or positive (blue colour) when inter-molecular contacts are shorter or longer than van der Waals separations, respectively (Fig. 4). The combination of d_e and d_i in the form of a 2D fingerprint plot (Fig. 5) gives the quantitative information of the inter-molecular inter-actions in the crystals. The largest proportion of the intermolecular inter-actions comprises of O—H inter-actions (43.4%) and appear as two symmetrical spikes on the 2D plot (Fig. 5).

C—O contacts are next comprising 21.0% of the total and appear as 'feathers' on the plot. This is followed by O—O inter-actions (14.1%) which occupy the upper central region. The H—H inter-actions have also a significant share comprising of 9.7% and are distributed over a wider range of distance. The C—H and N—O inter-actions make up 4.7% and 4.4% respectively and occupy *quasi* symmetrical regions on the fingerprint plots. The enrichment ratio (ER), which is used to analyze the propensity of chemical species to form inter-molecular inter-actions with themselves and with other species, was calculated, for each type of inter-action, using the method proposed by Jelsch et al. [83]. The ER values reveal that the C—O ···π-inter-actions are the most favored ones with a value of 1.61 followed by O—H and C—N inter-actions whose values are 1.29 and 1.26 respectively, which are significantly higher than unity. The H—H inter-actions have an ER value of 0.81 which indicates H, H pair tends to avoid contacts with each other, hence disfavored. Like this inter-action, rest of the inter-actions also have ER values significantly lower than unity and are thus considered as disfavored.

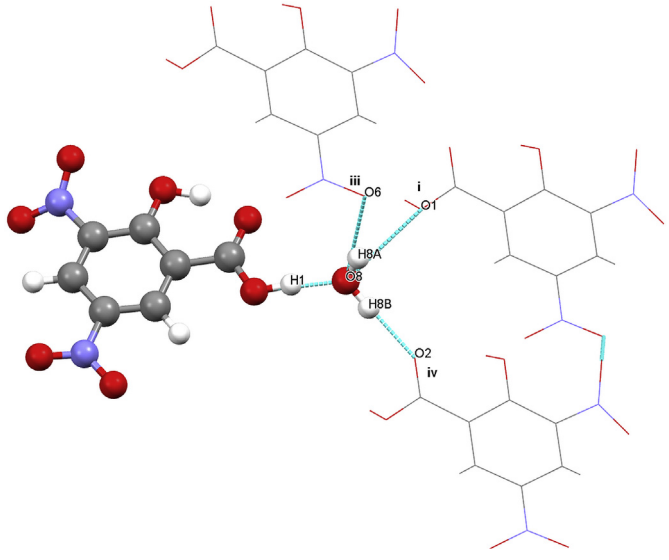

Fig. 3. A cluster of the molecules showing the role of water molecule in the molecular assembly (Symmetry codes same as in Table 2).

3.3. Electron density maps and topology of covalent bonds

Fig. 6 shows the static deformation density maps after multipolar refinement. The two oxygen atoms of N1 nitro group are slightly twisted out of the plane of the molecule; hence their electron density appears as diminished in the ring plane. The electron density peaks are well placed on the covalent bonds. The lone pairs on oxygen atoms need special emphasis. The lone pairs of two hydroxyl oxygen atoms are completely merged into a single lobe. However, the lone pairs of the carbonyl oxygen atom are bifurcated and form two separate lobes. Similar is the case of the oxygen atoms attached to the -NO_2 whose lone pairs form two separate lobes. Study has shown that there is a strong correlation between the shape and orientation of lone pairs and the directionality of the hydrogen bonds [84]. The electron density on the C—C bonds critical points (BCPs) of the aromatic ring ranges from 2.01 (2) to 2.26 (4) e/Å^3 (Table S1). The C1—C2 bond possesses the least amount of the electron density at the critical point whereas the C5—C6 has the highest accumulation on BCP. A similar trend is seen for the theoretical model. However, the minimum and maximum value of the electron density at the critical point for the aromatic C—C bonds is 1.99 (3) and 2.13 (3) e/Å^3 for theory. These values are in agreement with those available in the literature [50,85]. C1—C7 bond, which lies outside the aromatic ring plane by 0.086 (2) Å, has noticeably less electron density (1.81 (2) e/Å^3) at the critical point compared to its aromatic homologues in experimental model. This arises due to the fact of being attached to a highly electron withdrawing carboxylic acid group. The values of electron density at the two C—N BCPs slightly differ from each other. The C3—N1 bond has a slightly higher value of electron density at the critical point (1.78 (3) e/Å^3) as compared to the C5—N2 bond (1.73 (3) e/Å^3). Similar trends are also observed in the DFT calculations. The values of electron density at the four N—O bonds is almost same, *i.e.* 3.37(2) e/Å^3, differing only within the standard uncertainty. The same behaviour is observed for the theory. The difference between the electron density values at the two C7—O1 and C7—O2 bonds is noteworthy. In the case of former, which is a hydroxyl oxygen, the value is small 2.49 e/Å^3 as compared to the latter which is carbonyl oxygen and has an excess of electron density at BCP with a value of 2.85 e/Å^3. These values are consistent with the reported values for this class of bonds [50,85].

The Laplacian values have been listed in Table S1. The Laplacian of electron density is negative for all the covalent bonds. As observed in the case of electron density on BCPs, the charge is not uniformly concentrated on the aromatic C—C bonds. This is also reflected in the case of the Laplacian values which range from −16.21 e/Å^5 for C1—C2 to −19.26 e/Å^5 for C5—C6 in the experimental results. For the C—C bonds in the aromatic ring, the trend is harmonic with the value of electron densities. It is also observed that the Laplacian value is related to the length of the bond. For example, C1—C7 is a single bond and much larger than the aromatic bonds, hence as expected, it has lower electron density, lower Laplacian and small ellipticity. Similarly, for N—O bonds, the Laplacian values lie close to each other, ranging from −7.76 e/Å^5

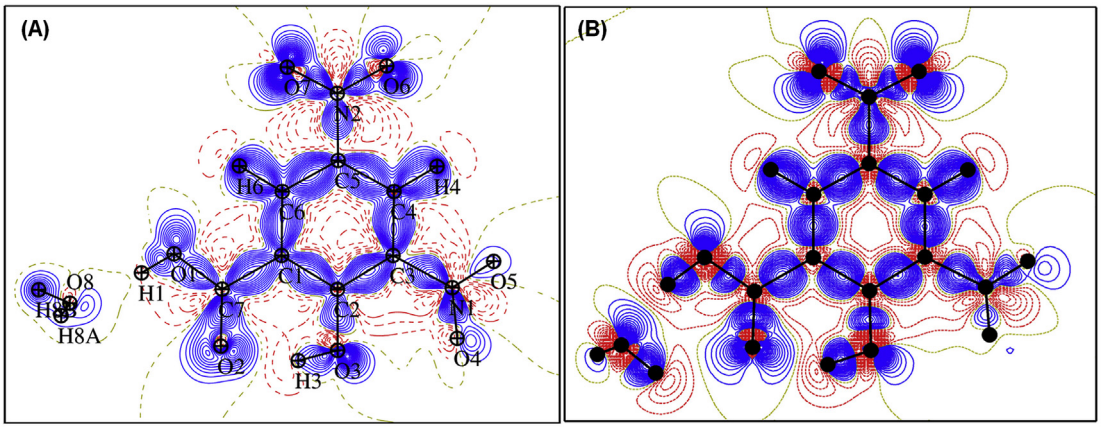

Fig. 4. A Hirshfeld surface with d_{norm} property showing the cluster of interacting molecules around the reference molecule.

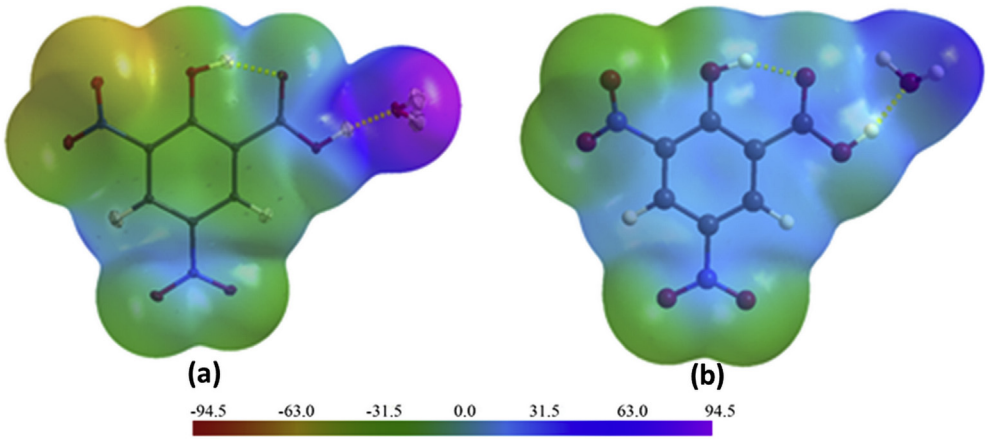

Fig. 5. (A) A 'fingerprint' plot of the molecule showing the percentage of various interactions. (B) Percentage of interactions shown as *pi* chart.

to −11.63 e/Å^5 respectively. The difference in charge concentration between the two C—O bonds of carboxyl moiety is also evident in the case of Laplacian values. The Laplacian value for the C7—O1 bond is −28.74 e/Å^5 while for C7—O2 it is −34.97 e/Å^5. As compared to these two bonds, the lower value of Laplacian for the C2—O3 bond (−21.24 e/Å^5) highlights the lower charge concentration and less dominance of potential energy on this bond. The Laplacian values for N—O bonds in two -NO_2 groups, established that there is more charge concentration on N1—O5 (−10.00 e/Å^5) and N1—O4 (−7.76 e/Å^5) bonds compared to N2—O6 (−11.63 e/Å^5) and N2—O7 (−9.37 e/Å^5) bonds respectively. This higher local electronic charge concentration on one -NO_2 group compared to other establishes its higher global reactivity towards electrophilic reagents. Hence the Laplacian of electron density provides one clue regarding the regioselective reduction of one nitro group.

3.4. Topology of non-covalent bonds

The topological analysis using Bader's theory of Atoms in Molecules [86] of the total electron density in the regions of intermolecular interactions was carried out to understand the strength of the hydrogen bonds and other intermolecular interactions. Table S2 lists the topological parameters of all the (3, −1) type interactions. All the listed interactions are characterized by positive Laplacian values. The interaction between the H1 atom of the DNSA moiety and O8 atom of water molecule is the strongest in terms hydrogen bond distance and the value of electron density at the bond critical point. The interaction also possesses very high values of energy densities. These parameters indicate that this interaction is very close to a covalent bond. This intermolecular interaction is even stronger than the intramolecular (O3—H3 ···O2) which also has a very short bond distances and very high values of electron density at the *bcp*. There are three other very strong intermolecular hydrogen bonds between O8—H8A···O6^{i}, O8—H8B···O2^{iv} and O3—H3 ···O5^{vii} (*symmetry codes as in Table 2) which have a significantly higher value of electron density at the BCP. The $\nabla^2_{cp} > 0$, $(G_{cp} + V_{cp}) > 0$ and $|V_{cp}|/G_{cp} < 1$ suggests that these interaction are pure close shell interaction [87]. The other two interactions C6—H6···H6^{ii} and C4—H4···O5^{iii} are relatively at longer distances and the value of electron density at the CPs is 0.05 e/Å^3 to 0.046 e/Å^3 respectively.

There are at least seven O—O interactions which deserve special attention. Although these interactions are weak in terms of interatomic distances and relatively less static electron density at the saddle points which lies in the range of 0.05to 0.01 e/Å^3, but the value of the Laplacian are quite reasonable ranging from 0.89 to o.38 e/Å^5. It suggests that these interactions are real ones and not the result of any errors in the modelling. Similar topological parameters for O—O inter-actions have already been reported by Pyziak et al. [88] There is also a strong inter-molecular H—H interaction whose length (2.13 Å) is much smaller than the sum of the van der Waal's radii (2.4 Å). The electron density at saddle

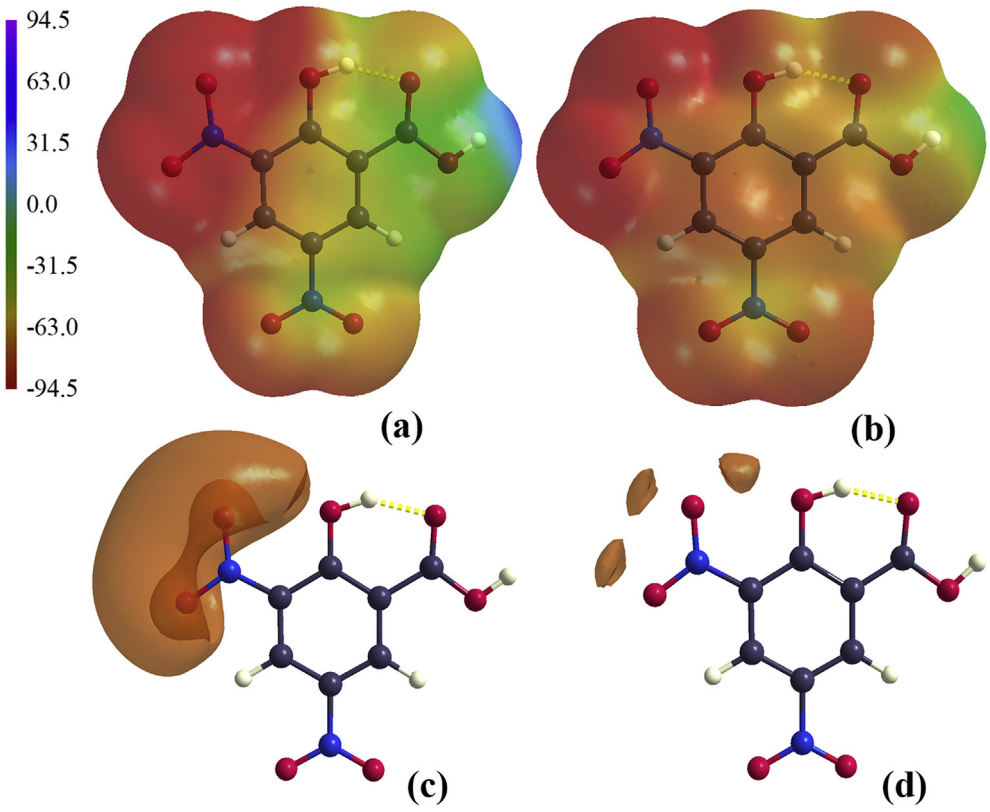

Fig. 6. Static electron density maps after Multipolar refinement (A) and from theoretical calculations (B). Contour level = 0.05e/Å^3.

point is lower (0.02 e/Å^3) as compared to other kind of interactions but the value is very significant in terms of hydrogen. The second derivative of electron density also has a significant value and authenticates the closed shell nature of the interaction.

3.5. Bader's charges

Using Bader's quantum theory of Atoms In Molecules [86], the QAIM charges derived from the integration of electron density over the atomic basins delimited by the zero-flux surfaces [86] have been listed in Table S3 for the multipolar and DFT calculations. For the experimental model, the total molecular volume is nearly equal to the one fourth of the unit cell volume and the integrated charge on the molecule is zero which highlights the overall high quality of the diffraction data and of the of refinements. Table S3 reveal that there is a remarkable consistency between the charges and the integrated volumes for the two models and the difference lies within the standard deviations. All the oxygen atoms bear partial negative charge. The highest concentration of negative charge is observed on the oxygen atoms of the carboxylic acid and the hydroxyl group. The oxygen atoms of the nitro group have also a partial negative character which seems slightly diminished probably due to the electronegative character of the nitrogen atoms. For the multipolar model, both the oxygen atoms attached to the N1 atom (O4 and O5) bear more negative charge than their N2 counterparts (O6 and O7). This gives an indication that the N1 nitro group will be preferentially reduced *i.e.* electrophilic reagents like H^+ will have more affinity for O4 and O5. Similarly, both nitrogen atoms have significant partial positive character and are electron depleted due to the higher electronegativity of O atoms. It is also noteworthy that both the nitrogen atoms have a nearly equal depletion of electrons albeit the difference between two models lies within approximately 0.1q. In the case of the carbon atoms, the C7 is found to be the most electron deficient owing to a carboxyl carbon. This is followed by the C2 atom which is also significantly deficient in electrons being bound to a hydroxyl group. The C3 and C5 atoms which are bound to nitro groups are moderately electron deficient. However, C4 and C6 are very slightly negative. The H1 and H3 atoms are most deficient of all H atoms owing to their covalent bonding with the highly electronegative oxygen atoms in each case. Moreover, the former is involved in the formation of a strong hydrogen bond with water molecule and the latter is involved in the formation of a strong intra-molecular hydrogen bond. H4 and H6 atoms are moderately deficient in electrons although in the MM they appear slightly more acidic than in the theoretical models. MM results shows that the total charge on water molecule is −0.12q whereas DFT model shows that water is neutral (0.04q).

3.6. Electrostatic potential

Electrostatic potential $V(r)$ distributions for the DNSA molecule taken from the crystal after MM and calculated using B3LYP are shown in Fig. 7(A) and (B) respectively as plotted onto 0.001 e/Å^3 electron density molecular surface. Most positive and most negative local values of ESP on molecular surface, identified as the $V_{S,max}$ and $V_{S,min}$, calculated using Multiwfn program [71] are given in Table S4. The partitioning of surface area in each ESP range on the electron density surface is given in Fig. S3. Due to the gas phase calculations, the values of theoretically calculated extrema of ESP are lower compared to the MM values (Table S4).

Similarly, the areas are more compact for the theoretically calculated electrostatic potential (Fig. S3). For both models, the majority of the surface area is occupied by the negative electrostatic potential (Fig. S4) which is found on two nitro groups. Similarly, for

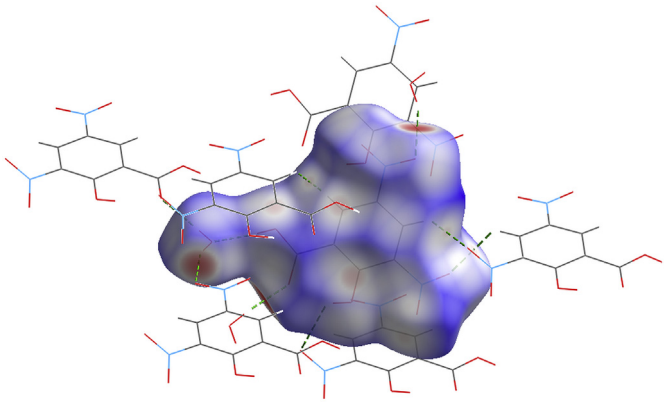

Fig. 7. Electrostatic potentials of DNSA molecule plotted onto the molecular 0.001 e/Å^3 electron density surface. (a) Experimental (b) Theoretical model in the gas phase. Colour ranges in kcal/mol. Images are created using MoleCoolQt software [89].

all three models, the global surface minimum is found on N1 nitro group and hydrogen of water molecules provide global surface maxima. The oxygen atoms of hydroxyl and of the carboxylic acid group also bear negative potential, but this is less pronounced probably due to the formation of an intramolecular hydrogen bonding between O2 and H3 and an intermolecular hydrogen bond involving H1 atom of DNSA moiety and the O8 atom of the water molecule which dilutes the negative charge concentration. As stated earlier, the first step in reduction of polynitro-aromatics in aqueous solution, whether it is chemical, anoxic or sediment-mediated reduction, involves the formation of radical anion and the regioselectivity is established by the first proton transfer to this radical anion (Scheme 2 of Ref. [1]. In order to understand the localization of negative charge (and hence the $V_{S,min}$) on this radical anion of DNSA, which will influence the site of protonation, we calculated the surface electrostatic potential of DNSA radical anion in gas phase and in continuum water (Fig. 8). The results of both calculations shows that the negative charge is mostly localized on two nitro groups and this localization is more on N1 nitro group compared to N2 nitro group. The same calculations in the presence of water molecule revealed similar findings (Fig. S5) except a small increment of negative charge on nitro groups due to charge (Bader) transfer of −0.0125e in gas phase and −0.0602e in continuum water from water to DNSA moiety at this level of theory. It can be inferred from these results, that during the reduction process of DNSA, the N1 nitro group will be reduced readily. Due to the Coulomb repulsion between electrons, the localization of negative charge is lower in gas phase compared to aqueous phase (Fig. 8 and Table S4). In continuum solvent phase, the delocalization of charge over molecule is lowered due to the favourable electric polarization induced by the solvent system: thus the more intense colours (Fig. 8(a)) for aqueous phase surface indicates the solvent promoted charge localization. In addition, the higher values of $V_{S,max}$ and $V_{S,min}$ for radical anion (Table S4) in solvent phase compared to the gas phase, highlights the charge polarization effects induced by solvent. The higher values of surface extrema on N1 nitro group in radical anion also compliments the findings of MM refinement for DNSA molecule in the crystalline phase.

4. Conclusion

In this study, we have carried out an experimental and theoretical charge density analysis of 3,5-di-nitro-salicylic acid monohydrate. Topological analysis has been carried out using Bader's QTAIM on the total experimental and theoretical electron density. Visualization of the electrostatic potential of DNSA molecule and its radical anion on the electron density surface provided a predictive diagnostic of regioselectivity. The Laplacian of electron density and the calculated atomic charges complimented the findings of electrostatic potential that the nitro group located at 3 position will be preferentially reduced compared to the nitro group at position 5. This work proves the strength of X-rays charge density methods to study the chemical reactivity of compounds.

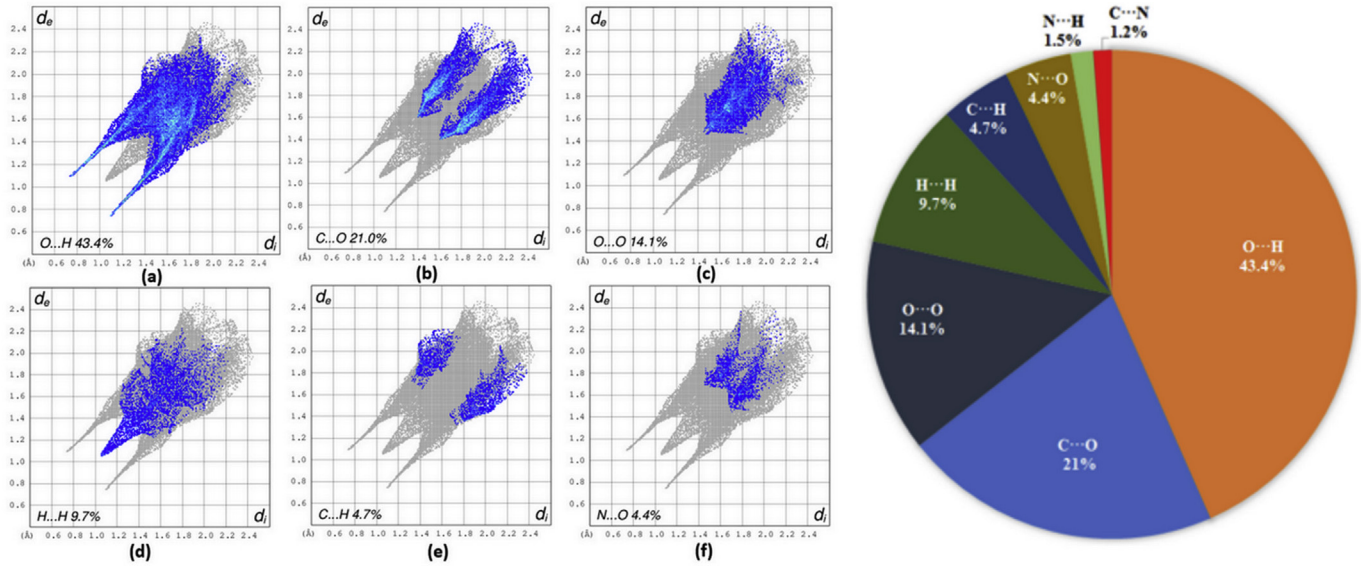

Fig. 8. Electrostatic potentials (in kcal/mol) of DNSA radical anion at ωB97XD/6-311++g(d,p) level of theory. (a) Calculated in continuum water and plotted onto the molecular 0.001 e/Å^3 electron density surface. (b) Calculated in the gas phase and plotted onto the molecular 0.001 e/Å^3 electron density surface. (c) Isosurfaces (−0.2 eÅ^{-3}) in continuum water (d) Isosurfaces (−0.2 eÅ^{-3}) in the gas phase.

Author contribution section

Sajida Noureen originally devised the project and procured materials and prepared the samples. Arshad Mehmood collected the data and wrote a part of the manuscript along with Aisha Faheem. Maqsood Ahmed carried out the refinements. Sajida Noureen reviewed the manuscript, removed errors and submitted. The authors declare no competing interests.

Acknowledgement

The authors gratefully acknowledge the Materials Chemistry Laboratory, Department of Chemistry, The Islamia University of Bahawalpur, Pakistan (http://mcl.iub.edu.pk/) for the provision of research facilities. This facility was established with a funding from the Higher Education Commission of Pakistan.

Appendix A. Supplementary data

Supplementary data related to this article can be found at https://doi.org/10.1016/j.molstruc.2020.128483.

References

[1] S.E. Barrows, C.J. Cramer, D.G. Truhlar, M.S. Elovitz, E.J. Weber, Environ. Sci. Technol. 30 (1996) 3028–3038.
[2] M. Kulkarni, A. Chaudhari, J. Environ. Manag. 85 (2007) 496–512.
[3] F.D. Marvin-Sikkema, J.A.M. de Bont, Appl. Microbiol. Biotechnol. 42 (1994) 499–507.
[4] S.B. Haderlein, K.W. Weissmahr, R.P. Schwarzenbach, Environ. Sci. Technol. 30 (1996) 612–622.
[5] M.A. Tarr, Chemical Degradation Methods for Wastes and Pollutants: Environmental and Industrial Applications, CRC Press, 2003.
[6] D.L. Macalady, P.G. Tratnyek, T.J. Grundl, J. Contam. Hydrol. 1 (1986) 1–28.
[7] E.J. Weber, R.L. Adams, Environ. Sci. Technol. 29 (1995) 1163–1170.
[8] J.C. Spain, Biodegradation of Nitroaromatic Compounds, Springer US, 2013.
[9] E.J. Olson, W.C. Isley, J.E. Brennan, C.J. Cramer, P. Bühlmann, J. Phys. Chem. C 119 (2015) 13088–13097.
[10] K.L. Phillips, P.C. Chiu, S.I. Sandler, Environ. Sci. Technol. 44 (2010) 7431–7436.
[11] S.-Y. Oh, P.C. Chiu, Environ. Sci. Technol. 43 (2009) 6983–6988.
[12] S.-Y. Oh, D.K. Cha, P.C. Chiu, Environ. Sci. Technol. 36 (2002) 2178–2184.
[13] R.G. Riefler, B.F. Smets, Environ. Sci. Technol. 34 (2000) 3900–3906.
[14] M.S. Elovitz, E.J. Weber, Environ. Sci. Technol. 33 (1999) 2617–2625.
[15] T.B. Hofstetter, C.G. Heijman, S.B. Haderlein, C. Holliger, R.P. Schwarzenbach, Environ. Sci. Technol. 33 (1999) 1479–1487.
[16] S.-Y. Oh, J.-G. Son, P.C. Chiu, Environmental Earth Sciences 73 (2015) 1813–1822.
[17] J. Hawari, F. Monteil-Rivera, N.N. Perreault, A. Halasz, L. Paquet, Z. Radovic-Hrapovic, S. Deschamps, S. Thiboutot, G. Ampleman, Chemosphere 119 (2015) 16–23.
[18] Y.Z. Song, Russ. J. Phys. Chem. 88 (2014) 1550–1558.
[19] H. Rojas, G. Borda, M. Brijaldo, P. Reyes, J. Valencia, React. Kinet. Mech. Catal. 105 (2012) 271–284.
[20] A.S. Mendkovich, M.A. Syroeshkin, L.V. Mikhalchenko, M.N. Mikhailov, A.I. Rusakov, #39 Gul, V.P. tyai, International Journal of Electrochemistry 2011 (2011).
[21] G.E. Diwani, S.E. Rafie, S. Hawash, Int. J. Environ. Sci. Technol. 6 (2009) 619–628.
[22] V.N. Leibzon, L.V. Michalchenko, M.Y. Leonova, V.P. Gultyai, Russ. Chem. Bull. 54 (2005) 1203–1207.
[23] V.N. Leibzon, A.P. Churilina, M.Y. Leonova, L.V. Mikhalchenko, A.K. Shakhnes, Russ. J. Electrochem. 36 (2000) 170–173.
[24] M. Pizzonero, L. Keller, F. Dumas, M. Ourevitch, G. Morgant, A. Spasojević-de Biré, G. Bogdanović, N.E. Ghermani, J. D'Angelo, J. Org. Chem. 69 (13) (2004) 4336–4350.
[25] D. Chopra, V.V. Zhurov, E.A. Zhurova, A.A. Pinkerton, J. Org. Chem. 74 (2009) 2389–2395.
[26] M. Ahmed, C. Jelsch, B. Guillot, C. Lecomte, S. Domagała, Cryst. Growth Des. 13 (2013a) 315–325.
[27] S.P. Thomas, K. Satheeshkumar, G. Mugesh, T.N. Guru Row, Chem. Eur J. 21 (2015) 1–9.
[28] A.M. Maharramov, K.T. Mahmudov, M.N. Kopylovich, A.J.L. Pombeiro, Non-covalent Interactions in the Synthesis and Design of New Compounds, Wiley, 2016.
[29] P.M. Pihko, Hydrogen Bonding in Organic Synthesis, Wiley, 2009.
[30] M. Tonogaki, T. Kawata, S. Ohba, Y. Iwata, I. Shibuya, Acta Crystallogr. B**49** (1993) 1031–1039.
[31] A. Puig-Molina, A. Alvarez-Larena, J.F. Piniella, S.T. Howard, F. Baert, Struct. Chem. 9 (1998) 395–402.
[32] R. Srinivasa Gopalan, P. Kumaradhas, G.U. Kulkarni, C.N.R. Rao, J. Mol. Struct. 521 (2000) 97–106.
[33] T.T.T. Bui, S. Dahaoui, C. Lecomte, G.R. Desiraju, E. Espinosa, Angew. Chem. Int. Ed. 48 (2009) 3838–3841.
[34] J.J. McKinnon, D. Jayatilaka, M.A. Spackman, Chem. Commun. (2007) 3814–3816.
[35] P. Munshi, T.N. Guru Row, CrystEngComm 7 (2005) 608–611.
[36] C.G. Gianopoulos, B. Zarychta, S. Cenedese, V.V. Zhurov, A.A. Pinkerton, J. Phys. Chem. A 120 (2016) 4059–4070.
[37] E. Espinosa, C. Lecomte, E. Molins, Chem. Phys. Lett. 300 (1999) 745–748.
[38] L.C. Wu, W.C. Chung, C.C. Wang, G.H. Lee, S.I. Lu, Y. Wang, Phys. Chem. Chem. Phys. 17 (2015) 14177–14184.
[39] C. Gatti, E. May, R. Destro, F. Cargnoni, J. Phys. Chem. A 106 (2002) 2707–2720.
[40] A. Ranganathan, G.U. Kulkarni, C.N.R. Rao, J. Mol. Struct. 656 (2003) 249–263.
[41] N. Singh, I.M. Khan, A. Ahmad, S. Javed, J. Mol. Liq. 191 (2014) 142–150.
[42] G. Smith, U.D. Wermuth, J.M. White, Acta Crystallogr. E**57** (2001) o1036–o1038.
[43] H.T. Varghese, C.Y. Panicker, D. Philip, J. Chowdhury, M. Ghosh, J. Raman Spectrosc. 38 (2007) 323–331.
[44] G. Smith, D. Lynch, K. Byriel, C. Kennard, Aust. J. Chem. 48 (1995) 1133–1149.
[45] G. Smith, U.D. Wermuth, P.C. Healy, J.M. White, J. Chem. Crystallogr. 41 (2011) 1649–1662.
[46] G.L. Miller, Anal. Chem. 31 (1959) 426–428.
[47] H. Lindsay, Potato Res. 16 (1973) 176–179.
[48] J.B. Sumner, W.C.V. Noback, J. Biol. Chem. 62 (1924) 287–290.
[49] C.R. Groom, I.J. Bruno, M.P. Lightfoot, S.C. Ward, Acta Crystallogr. B**72** (2016) 171–179.
[50] V.V. Zhurov, A.A. Pinkerton, J. Phys. Chem. A 119 (2015) 13092–13100.
[51] J. Cosier, A.M. Glazer, J. Appl. Crystallogr. 19 (1986) 105–107.
[52] Bruker, APEX3, SAINT and SADABS, Bruker AXS Inc., Madison, Wisconsin, USA, 2016.
[53] L. Krause, R. Herbst-Irmer, G.M. Sheldrick, D. Stalke, J. Appl. Crystallogr. 48 (2015) 3–10.
[54] A. Altomare, G. Cascarano, C. Giacovazzo, A. Guagliardi, J. Appl. Crystallogr. 26 (1993) 343–350.
[55] G.M. Sheldrick, Acta Crystallogr. C**71** (2015) 3–8.
[56] L.J. Farrugia, J. Appl. Crystallogr. 45 (2012) 849–854.
[57] C. Jelsch, B. Guillot, A. Lagoutte, C. Lecomte, J. Appl. Crystallogr. 38 (2005) 38–54.
[58] F.H. Allen, I.J. Bruno, Acta Crystallogr. B**66** (2010) 380–386.
[59] M.J. Frisch, G.W. Trucks, H.B. Schlegel, G.E. Scuseria, M.A. Robb, J.R. Cheeseman, G. Scalmani, V. Barone, B. Mennucci, G.A. Petersson, H. Nakatsuji, M. Caricato, X. Li, H.P. Hratchian, A.F. Izmaylov, J. Bloino, G. Zheng, J.L. Sonnenberg, M. Hada, M. Ehara, K. Toyota, R. Fukuda, J. Hasegawa, M. Ishida, T. Nakajima, Y. Honda, O. Kitao, H. Nakai, T. Vreven, J.A. Montgomery Jr., J.E. Peralta, F. Ogliaro, M.J. Bearpark, J. Heyd, E.N. Brothers, K.N. Kudin, V.N. Staroverov, R. Kobayashi, J. Normand, K. Raghavachari, A.P. Rendell, J.C. Burant, S.S. Iyengar, J. Tomasi, M. Cossi, N. Rega, N.J. Millam, M. Klene, J.E. Knox, J.B. Cross, V. Bakken, C. Adamo, J. Jaramillo, R. Gomperts, R.E. Stratmann, O. Yazyev, A.J. Austin, R. Cammi, C. Pomelli, J.W. Ochterski, R.L. Martin, K. Morokuma, V.G. Zakrzewski, G.A. Voth, P. Salvador, J.J. Dannenberg, S. Dapprich, A.D. Daniels, Ö. Farka, J.B. Foresman, J.V. Ortiz, J. Cioslowski, D.J. Fox, Gaussian 09, 2009.
[60] A.Ø. Madsen, H.O. Sørensen, C. Flensburg, R.F. Stewart, S. Larsen, Acta Crystallogr. A**60** (2004) 550–561.
[61] P. Roversi, R. Destro, Chem. Phys. Lett. 386 (2004) 472–478.
[62] A.E. Whitten, M.A. Spackman, Acta Crystallogr. B**62** (2006) 875–888.
[63] A.A. Hoser, P.M. Dominiak, K. Wozniak, Acta Crystallogr. A**65** (2009) 300–311.
[64] A.Ø. Madsen, J. Appl. Crystallogr. 39 (2006) 757–758.
[65] V.V. Zhurov, E.A. Zhurova, A.A. Pinkerton, J. Appl. Crystallogr. 41 (2008) 340–349.
[66] N.K. Hansen, P. Coppens, Acta Crystallogr. A**34** (1978) 909–921.
[67] A. Volkov, Y.A. Abramov, P. Coppens, Acta Crystallogr. A**57** (2001) 272–282.
[68] P. Hohenberg, W. Kohn, Phys. Rev. 136 (1964) B864–B871.
[69] R. Krishnan, J.S. Binkley, R. Seeger, J.A. Pople, J. Chem. Phys. 72 (1980) 650–654.
[70] G.B. Bacskay, Chem. Phys. 61 (1981) 385–404.
[71] T. Lu, F. Chen, J. Comput. Chem. 33 (2012) 580–592.
[72] D. Vega, D. Almeida, J. Comput. Methods Sci. Eng. 14 (2014) 131–136.
[73] J.P. Perdew, K. Burke, M. Ernzerhof, Phys. Rev. Lett. 77 (1996) 3865–3868.
[74] J. Tomasi, B. Mennucci, R. Cammi, Chem. Rev. 105 (2005) 2999–3094.
[75] F.L. Hirshfeld, Theor. Chim. Acta 44 (1977) 129–138.
[76] M.A. Spackman, P.G. Byrom, Chem. Phys. Lett. 267 (1997) 215–220.
[77] M.A. Spackman, J.J. McKinnon, CrystEngComm 4 (2002) 378–392.
[78] J.J. McKinnon, F.P.A. Fabbiani, M.A. Spackman, Cryst. Growth Des. 7 (2007) 755–769.
[79] M.A. Spackman, D. Jayatilaka, CrystEngComm 11 (2009) 19–32.
[80] M.A. Spackman, J.J. McKinnon, D. Jayatilaka, CrystEngComm 10 (2008) 377–388.
[81] J.J. McKinnon, M.A. Spackman, A.S. Mitchell, Acta Crystallogr. B**60** (2004) 627–668.
[82] S.K. Wolff, D.J. Grimwood, J.J. McKinnon, M.J. Turner, D. Jayatilaka,

M.A. Spackman, CrystalExplorer, 2012, Version Version 3.1.
[83] C. Jelsch, K. Ejsmont, L. Huder, IUCrJ 1 (2014) 119–128.
[84] M. Ahmed, M. Yar, A. Nassour, B. Guillot, C. Lecomte, C. Jelsch, J. Phys. Chem. A 117 (2013b) 14267–14275.
[85] D.S. Arputharaj, V.R. Hathwar, T.N. Guru Row, P. Kumaradhas, Cryst. Growth Des. 12 (2012) 4357–4366.
[86] R.F.W. Bader, Atoms in Molecules: A Quantum Theory, Clarendon Press, 1994.
[87] E. Espinosa, I. Alkorta, J. Elguero, E. Molins, J. Chem. Phys. 117 (2002) 5529–5542.
[88] M. Pyziak, J. Pyziak, M. Hoffmann, M. Kubicki, Cryst. Growth Des. 15 (2015) 5223–5232.
[89] C.B. Hübschle, B. Dittrich, J. Appl. Crystallogr. 44 (2011) 238–240.